1   **The neural basis of temperature-driven host seeking in the human threadworm**
2   ***Strongyloides stercoralis***
3
4   Astra S. Bryant[1], Felicitas Ruiz[1†], Joon Ha Lee[1‡], Elissa A. Hallem[1,2]
5
6   [1] Department of Microbiology, Immunology, and Molecular Genetics, University of
7   California, Los Angeles, Los Angeles, CA 90095
8
9   [2] Molecular Biology Institute, University of California, Los Angeles, Los Angeles, CA
10   90095
11
12   [†] Present address: Molecular & Cellular Biology in Seattle Program, Fred Hutchinson
13   Cancer Research Center, 1100 Fairview Ave N, Seattle, WA 98115
14
15   [‡] Present address: Yale Interdepartmental Neuroscience Program, Yale University, 260
16   Whitney Ave, New Haven, CT 06511

Abstract

17

18 Soil-transmitted parasitic nematodes infect approximately one billion people and are a
19 major cause of morbidity worldwide[1–8]. The infective larvae (iL3s) of these parasites
20 actively search for hosts in a poorly understood, sensory-driven process that requires
21 thermal cues[9,10]. Here, we describe the neural basis of temperature-driven host seeking
22 in parasitic nematodes using the human threadworm *Strongyloides stercoralis.* We
23 show that *S. stercoralis* thermosensation is mediated by the AFD neurons, a
24 thermosensory neuron class that is conserved between parasitic and free-living
25 nematodes[11]. We demonstrate that *S. stercoralis* AFD displays parasite-specific
26 adaptations that enable both nonlinear and linear encoding of temperatures up to
27 human body temperature. Furthermore, we describe a novel thermosensory behavior in
28 which *S. stercoralis* iL3s generate spontaneous reversals of temperature preference at
29 below-body temperatures. Finally, we identify three thermoreceptors selectively
30 expressed in *S. stercoralis* AFD that display parasite-specific sensitivities to human
31 body temperatures and likely enable temperature-driven host seeking by iL3s. Our
32 results are the first direct evidence that the sensory neurons of soil-transmitted parasitic
33 nematodes exhibit parasite-specific neural adaptations and sensory coding strategies
34 that allow them to target human hosts, a finding with important implications for efforts to
35 develop new therapeutic strategies for nematode control.

36 Soil-transmitted gastrointestinal helminths such as the human threadworm
37 *Strongyloides stercoralis* and the hookworms *Ancylostoma duodenale* and *Necator*
38 *americanus* are a major source of neglected disease affecting the world's most
39 socioeconomically depressed communities[1–8]. These parasites can cause chronic
40 gastrointestinal distress as well as stunted growth and cognitive impairment in children.
41 *S. stercoralis* is estimated to infect at least 610 million people worldwide[12]; infections
42 can be fatal for immunosuppressed individuals[13–15]. Current therapeutics against
43 parasitic nematodes exclusively target ongoing infections. These anthelmintic drugs
44 have variable efficacy at clearing infections, and the lack of prophylactic treatments
45 results in high reinfection rates[16–19]. Additionally, repeated dosage with anthelmintics
46 may give rise to drug-resistant nematodes[16–18], underscoring the need for preventative
47 strategies. A mechanistic understanding of how parasitic nematodes locate hosts may
48 enable the development of new therapeutic approaches to preventing infections.
49
50 For parasitic nematodes that infect humans and other mammals, host detection and
51 subsequent infection require thermal cues[10,20]. Mammalian-parasitic iL3s, including
52 those of *S. stercoralis*, display robust attraction to mammalian body heat when exposed
53 to temperatures above an ambient cultivation temperature (T_C; Fig. 1a)[10,11]. This
54 positive thermotaxis behavior is specific to mammalian-parasitic nematodes: insect-
55 parasitic nematodes and the free-living model nematode *Caenorhabditis elegans* are
56 not attracted to mammalian body heat[10]. Indeed, exposure to temperatures above T_C
57 drives either negative thermotaxis or noxious heat avoidance by *C. elegans* adults[21–26].
58 The molecular and neural basis of *C. elegans* thermosensation has been extensively
59 studied[21,24,26,27]. However, virtually nothing is known about the neural mechanisms that
60 underlie thermosensory behaviors in parasitic nematodes or any other endoparasitic
61 animal. More generally, although sensory neuroanatomy is broadly conserved across
62 free-living and parasitic nematode species[9], the neural mechanisms that enable
63 nematodes to engage in species-specific behaviors such as host seeking have not been
64 identified.
65
66 **Genetic identification of *S. stercoralis* thermosensory neurons**
67 To understand the neural mechanisms of thermosensation in *S. stercoralis* iL3s, we first
68 used a genetic approach to identify the primary thermosensory neurons of *S.*
69 *stercoralis*. The identification of thermosensory neurons in *S. stercoralis* has been an
70 historical challenge due to morphological differences in sensory neuroanatomy that
71 complicate anatomical comparisons between *S. stercoralis* and *C. elegans*[11]. In
72 *C. elegans*, the AFD sensory neuron pair provides the primary thermosensory drive for
73 thermotaxis navigation[26,28–31]. *C. elegans* AFD neurons are structurally defined by
74 "finger-like" microvilli that emerge from the dendritic ends at the nose of the animal and
75 are thought to enhance neuronal sensitivity to temperature fluctuations[26]. *S. stercoralis*
76 lacks sensory neurons with these "finger-like" structures[32]. The closest anatomical
77 homologs appear to be the multi-layered "lamellae" of the ALD neurons, which are the
78 only elaborate sensory endings in the *S. stercoralis* amphid sensory organs[32]. However,
79 due to both variations in the arrangement of the cell bodies that comprise the amphid
80 sensory organs (13 soma for *S. stercoralis* versus 12 soma for *C. elegans*) and life-
81 stage-specific changes in the morphology of sensory neurons, whether ALD neurons

82 are homologs of the *C. elegans* AFD thermosensory neurons or AWC chemosensory
83 neurons (the other *C. elegans* amphid neurons with elaborate sensory endings) has
84 been unclear[11,32–34].

85

86 In *C. elegans*, the receptor-type guanylyl cyclases (rGCs) GCY-8, GCY-18, and GCY-23
87 are expressed selectively in *C. elegans* AFD, contribute to thermosensation via
88 activation of the cyclic GMP-gated channel subunit TAX-4, and are used as AFD-
89 specific genetic markers[31,35–38]. The *S. stercoralis* TAX-4 homolog, *Ss*-TAX-4, is
90 required for positive thermotaxis by iL3s[10,20]. Thus, parasite homologs of the AFD-rGCs
91 may serve as molecular markers for AFD-specific function, permitting the genetic
92 identification of the sensory neurons that drive the temperature-driven movements of *S.*
93 *stercoralis* iL3s. The use of parasite homologs is necessary as *C. elegans* transgenes
94 and regulatory elements are generally inactive in *Strongyloides* species[39–41].

95

96 We used BLASTP to identify homologs of the three *C. elegans* AFD-rGCs in *S.*
97 *stercoralis* and the closely related rat parasite *Strongyloides ratti*. The genomes of *S.*
98 *stercoralis* and *S. ratti* each contain three putative AFD-rGCs (Fig. 1b). A phylogenetic
99 comparison between the nine protein sequences revealed that although there is clear 1-
100 to-1 homology between the *Strongyloides* species, all six *Strongyloides* sequences are
101 most homologous to *C. elegans* GCY-23 (Fig. 1b, Fig. S1a). Based on protein sequence
102 homology, we therefore named the *S. stercoralis* and *S. ratti* homologs GCY-23.1,
103 GCY-23.2, and GCY-23.3. We then extracted promoter sequences for the three
104 *S. stercoralis* rGCs, as well as *Sr*-GCY-23.2, and found that all four promoters drive
105 strong transgene expression in a single *Ss-tax-4*-positive head neuron pair in
106 *S. stercoralis* iL3s (Fig. 1c, Fig. S1b,c). Using confocal microscopy, we found that this
107 neuron pair displays elaborate structures at the nose tip that strongly resemble electron
108 microscopy reconstructions of the ALD lamellae (Fig. 1c)[33,34]. Based on genetic
109 homology, we thus identified the *S. stercoralis* ALD neurons as homologs of the
110 *C. elegans* AFD neurons (and hereafter refer to them as *S. stercoralis* AFD neurons, or
111 *Ss*-AFD).

112

113 **S. stercoralis AFD neurons are required for heat seeking**
114 To test whether the *Ss*-AFD neurons are required for the attraction of *S. stercoralis* iL3s
115 to mammalian body temperatures, we chemogenetically silenced them via AFD-specific
116 expression of the *Drosophila* histamine-gated chloride channel HisCl1[42], which we
117 codon-optimized for *Strongyloides* (*Sr-gcy-23.2p::strHisCl1*, Fig. S2a). We found that
118 silencing *Ss*-AFD reduced the migration of iL3s toward temperatures approximating
119 mammalian body heat, blocked temperature-driven increases in worm speed, and
120 reduced thermal drive-dependent inhibition of local search (Fig. 1d, Fig. S2b). Our
121 results establish single neuron genetic targeting for the first time in a non-
122 *Caenorhabditis* nematode and demonstrate that the *Ss*-AFD neurons are required for
123 the heat-seeking behavior of iL3s, thus confirming the impact of *Ss*-ALD laser
124 ablation[33]. Notably, our results indicate that *S. stercoralis* and *C. elegans* rely on a
125 homologous primary sensory neuron pair to drive distinct behaviors in response to
126 temperatures above ambient: negative thermotaxis by *C. elegans* adults[26] and positive
127 thermotaxis by *S. stercoralis* iL3s.

128
Novel encoding of naturalistic warming stimuli by *S. stercoralis* AFD neurons

130 Do temperature-driven responses in *Ss*-AFD display species-specific adaptations, or is
131 AFD encoding of temperature conserved between parasitic and free-living nematodes?
132 We generated iL3s expressing yellow cameleon YC3.60[43] in *Ss*-AFD, which allowed us
133 to image neural activity for the first time in a non-*Caenorhabditis* nematode. We
134 designed thermal stimuli that mimic the temperatures experienced by iL3s engaged in
135 positive thermotaxis toward host body temperatures; these naturalistic warming stimuli
136 were delivered to immobilized worms via a custom PID-controlled thermal stimulator
137 (0.025 °C/s; Fig. S3a,b). We then imaged from *S. stercoralis* AFD and *C. elegans* AFD
138 under the same experimental conditions. Consistent with previous findings[26,36,44,45],
139 naturalistic warming stimuli drive large depolarizations in *C. elegans* AFD (*Ce*-AFD)
140 above a response threshold (T^*_{AFD}) set near cultivation temperature (T_C; Fig. 2a,b). *Ce*-
141 AFD monotonically and nonlinearly encodes temperature deviations near T_C, such that
142 the lowest *Ce*-AFD response is driven by the coolest temperature in the thermal
143 stimulus (Fig. 2c) and the *Ce*-AFD response is positively correlated with increasing
144 temperature only in a narrow temperature range near T^*_{AFD} and not at warmer
145 temperatures (Fig. 2d-h).

146

147 In contrast, temperature-driven responses in *Ss*-AFD encode different features of the
148 thermal stimulus and display multiple parasite-specific adaptations. *Ss*-AFD also has a
149 response threshold near T_C (Fig. 2a,b). However, the *Ss*-AFD response at T^*_{AFD} is
150 dominated by a warming-triggered inhibition, such that the temperature that elicits the
151 lowest *Ss*-AFD response is near T_C (Fig. 2c). This warming-triggered inhibition results in
152 a negative monotonic relationship between temperature and *Ss*-AFD activity near T_C
153 (Fig. 2d,e). Following warming-triggered inhibition, *Ss*-AFD responses show near-linear
154 positive encoding of temperatures ranging from near T_C to above human body
155 temperature, with peak excitatory responses driven by the warmest temperature in the
156 stimulus (Fig. 2f-h, Fig. S4). These parasite-specific response properties provide a
157 mechanism for *Ss*-AFD to encode additional information and differentiate between a
158 broad range of host and environmental temperatures, and are likely critical for the ability
159 of iL3s to host seek over relatively long distances[9]. The observation that natural
160 behaviors arise from species-specific functional adaptations in developmentally
161 homologous neural structures is a central tenet of neuroethology. However, the nature
162 of such functional adaptations remains poorly understood. Our results demonstrate that
163 the parasitic behaviors of soil-transmitted nematodes emerge from functional
164 adaptations at the earliest stages of sensory information processing within the
165 conserved nematode nervous system.

166

167 Next, we tested the response of *Ss*-AFD and *Ce*-AFD to rapid warming temperature
168 ramps (0.1 °C/s; Fig. S5a-c). Consistent with previous reports[46], *Ce*-AFD responses are
169 similar across ramp rates. In contrast, the shape of *Ss*-AFD responses is partially
170 dependent on ramp steepness. Rapid temperature ramps are less likely to produce
171 warming-triggered inhibition, such that for the majority of iL3s, the coolest temperature
172 in the rapid stimulus ramp drives the lowest *Ss*-AFD response (Fig. S5c-e). T^*_{AFD} is not
173 affected by ramp speed (Fig. S5f). Furthermore, *Ss*-AFD maintains both near-linear

174 positive encoding of temperature above ~T_C in response to rapid ramp speeds and a
175 peak Ca^{2+} response at the warmest temperatures in the stimulus (Fig. S5g,h). These
176 results suggest that the mechanisms of warming-triggered inhibition in *Ss*-AFD may be
177 partially separate from the mechanisms of warming-triggered depolarizations and the
178 setting of thermal response threshold. Warming-triggered inhibitory responses have not
179 been reported previously in nematodes and thus may represent a parasite-specific
180 molecular mechanism for encoding thermosensory signals. Taken together, our
181 observations highlight the potential of elements in the *Ss*-AFD thermotransduction
182 pathway as novel targets for parasite-specific therapeutic interventions.
183
184 **Ss-AFD responses are regulated by cultivation temperature**
185 The thermotaxis behaviors of both *C. elegans* and *S. stercoralis* are regulated by
186 changes in cultivation temperature[11,26]. In *C. elegans*, exposing animals to a new
187 cultivation temperature shifts the thermal threshold of AFD toward the new T_C[26,36,44,45].
188 To determine whether responses in *Ss*-AFD and *Ce*-AFD display similar T_C-dependent
189 changes, we cultivated worms overnight at 15°C, then exposed them to naturalistic
190 thermal stimuli that were shifted toward cooler temperatures (Fig. S3c). Cultivation at
191 15°C shifts T^*_{AFD} toward cooler temperatures in both *Ss*-AFD and *Ce*-AFD (Fig. S6a-d).
192 The downward shift in thermal threshold does not eliminate the unique properties of the
193 *Ss*-AFD response. The response at the cooler T^*_{AFD} is still dominated by warming-
194 triggered inhibition, with a peak hyperpolarization just above T^*_{AFD} (Fig. S6e), and a
195 peak depolarization in response to the warmest temperature in the stimulus (Fig. S6f).
196 Notably, despite the shift in T^*_{AFD} toward cooler temperatures, *Ss*-AFD still responds
197 near-linearly to temperatures up to host body temperatures (Fig. S6c), consistent with
198 earlier behavioral results demonstrating that *S. stercoralis* iL3s cultivated at 15°C
199 engage in robust positive thermotaxis toward skin temperatures[10]. The preservation of
200 near-linear encoding at host body temperatures, combined with experience-dependent
201 expansions in the dynamic range of *Ss*-AFD thermosensitivity, further supports a model
202 in which parasite-specific adaptations in sensory information processing pathways
203 actuate the ability of iL3s to host seek across a range of ethological contexts.
204
205 **Characterizing negative thermotaxis behaviors of *S. stercoralis* iL3s**
206 Besides attraction to host body temperatures, mammalian-parasitic iL3s display
207 negative thermotaxis: migration toward cooler temperatures when exposed to
208 temperatures below their ambient cultivation temperature[10]. Previously, negative
209 thermotaxis was measured exclusively using iL3s exposed to a ~20-34°C gradient[10];
210 here we expand on those initial observations by measuring migration in a ~12-22°C
211 gradient (Fig. S7). When placed at 20°C or 17°C, iL3s cultivated at 23°C display
212 negative thermotaxis, accumulating near ~16°C (Fig. S7a). These migration patterns
213 are regulated by recent experience, such that iL3s cultivated at 15°C for at least 2 hours
214 accumulate at cooler temperatures than iL3s cultivated at 23°C (Fig. S7b-d). Does
215 accumulation near ~16°C represent a *bona fide* preferred temperature? If yes, iL3s
216 placed below 16°C should navigate up thermal gradients toward their "preferred"
217 temperature. In fact, iL3s placed at 14°C in a ~12-22°C gradient remain at cooler
218 temperatures, regardless of cultivation temperature (Fig. S7). Thus, *S. stercoralis* iL3s
219 do not appear to have a single preferred "cool" temperature. Rather, negative

220 thermotaxis appears to be regulated by the strength of thermal drive, which decays as a
221 function of deviations from T_C, similar to positive thermotaxis[10].
222

Ss-AFD mediates negative thermotaxis via an *Ss-tax-4* signaling cascade

224 Positive and negative thermotaxis behaviors represent distinct iL3 behavioral modes,
225 and it was not known whether these behaviors are regulated by the same signaling
226 cascades and primary sensory neurons. We found that CRISPR/Cas9-mediated
227 targeted mutagenesis of *Ss-tax-4*[47] and HisCl1-mediated silencing of *Ss*-AFD activity
228 both abolish negative thermotaxis by iL3s (Fig. S8a,b), similar to positive thermotaxis
229 (Fig. 1d)[10]. In *C. elegans*, positive and negative thermotaxis behaviors toward T_C also
230 rely on *Ce-tax-4*-dependent sensory transduction in *Ce*-AFD[26,36,48,49]. Thus, our results
231 provide additional evidence that the opposing thermosensory behaviors of *S. stercoralis*
232 iL3s and *C. elegans* adults reflect adaptations of a broadly conserved nematode
233 thermosensory circuit.
234

235 Next, we tested the effect of cooling temperature ramps on *Ss*-AFD activity, compared
236 to *Ce*-AFD. Delivery of a rapidly cooling temperature ramp (range: 22-13°C, Fig. S8c),
237 drives near-linear cooling-mediated hyperpolarizations in both *Ce*-AFD and *Ss*-AFD
238 (Fig. S8d,e). These results suggest that cooling-mediated inhibition of AFD corresponds
239 to opposing behaviors in free-living and parasitic nematodes: negative thermotaxis
240 toward below-ambient temperatures for *S. stercoralis* iL3s versus positive thermotaxis
241 toward the "remembered" cultivation temperature for *C. elegans* adults.
242

S. stercoralis iL3s display a unique "reversal" behavior

244 When navigating in the environment, *S. stercoralis* iL3s likely encounter temperature
245 gradients that terminate well below host body temperature and do not reflect the
246 presence of a host animal (*e.g.,* sun-warmed soil). Do iL3s have a mechanism that
247 enables them to avoid accumulation at these "false positive" heat sources? To address
248 this question, we examined the behavior of iL3s in temperature gradients that are
249 warmer than ambient but well below host body heat. We first exposed iL3s cultivated at
250 23°C to temperature ramps ranging from 15-25°C (T_{start} = 23°C). Under these
251 conditions, most iL3s initially engage in positive thermotaxis and accumulate at the
252 warmest temperature in the gradient, consistent with the behaviors of iL3s in thermal
253 gradients that end near host body temperature[10]. However, unlike our observations with
254 warmer gradients, we found that some of these heat-seeking iL3s will, within minutes,
255 abruptly transition to sustained negative thermotaxis (Fig. 3a; median percent of heat-
256 seeking iL3s that reverse = 35%; median dwell time at T_{max} = 216 s). Worms cultivated
257 at 15°C display similar "reversal" behaviors (Fig. 3b; median dwell time at T_{max} = 126 s),
258 with increased reversal frequencies observed in thermal gradients that terminate closer
259 to T_C (Fig. 3c; median percent of heat-seeking iL3s that reverse in a 15-25°C gradient =
260 3.46%, median percent of heat-seeking iL3s that reverse in a 12-22°C gradient =
261 97.25%). Across cultivation temperatures, reversal behaviors were only ever observed
262 in thermal gradients that end well below host body temperature[10]. Thus, the likelihood
263 that iL3s will transition from positive to negative thermotaxis is modulated by both
264 cultivation temperature and the assay gradient (Fig. 3c). This rapid reversal of thermal
265 preferences appears to be parasite-specific, as *C. elegans* behavioral preferences only

266 change on the timescale of hours, not minutes[21,26,50]. Reversal behaviors likely allow
267 iL3s to rapidly abandon an erroneous attraction to non-host heat sources. Our results
268 identify a new component of temperature-driven host seeking, and indicate that soil-
269 transmitted parasitic nematodes rely on a host-seeking strategy that flexibly adjusts in
270 response to sensory experience.
271
272 To test for neural correlates of the reversal behavior, we designed imaging stimuli that
273 mimicked reversal trajectories (Fig. 3d), then quantified Ss-AFD responses at the
274 transition between an initial warming ramp and sustained exposure to a maximum
275 temperature (T_{max}). We found that Ss-AFD responses at T_{max} rapidly (within ~30 s)
276 adapted toward the baseline T_C response (Fig. 3e-h; median early response at T_{max} = -
277 16.8% $\Delta R/R_{Tc}$, median late response T_{max} = 2.9% $\Delta R/R_{Tc}$). To test whether this rapid
278 adaptation may be a neural correlate of reversal behavior, we compared Ss-AFD
279 responses to a range of T_{max} values associated with a range of reversal rates: 22°C
280 (many reversals), 26°C (some reversals) and 32°C (no reversals). We found that the
281 degree of Ss-AFD response adaptation approximates the likelihood that thermal stimuli
282 would drive reversal behaviors: for iL3s cultivated at 15°C, Ss-AFD responses to
283 steady-state thermal stimuli strongly adapt at 22°C, moderately adapt at 26°C, and do
284 not adapt at 32°C (Fig. 3f-h). This result suggests that rapid adaptation in the Ss-AFD
285 response to some, but not all, temperature stimuli may underlie the ability of iL3s to
286 selectively engage in reversal behaviors.
287
288 Most of the highly adapting Ss-AFD responses are warming-triggered
289 hyperpolarizations. We therefore tested whether rapid adaptation reflects a general
290 inability of Ss-AFD to maintain prolonged hyperpolarization. Cooling temperature ramps
291 from 22-13°C drive Ss-AFD hyperpolarizations of similar magnitude to non-adapted
292 warming-triggered hyperpolarizations at 22°C, but do not display rapid adaptation (Fig.
293 S9a,b). These results suggest that Ss-AFD response adaptation is likely a consequence
294 of the thermal stimuli themselves rather than the direction of the Ss-AFD response, and
295 that distinct processes cause cooling- and warming-triggered hyperpolarizations in Ss-
296 AFD. In $C.$ $elegans$, although Ce-AFD can display minutes-long adaptation to recent
297 temperature experiences[26,36,46,51], these changes do not appear to affect behavioral
298 temperature preferences, which are thought to adapt primarily on longer (hours-long)
299 timescales[26,46]. Thus, our results suggest that iL3 reversal behavior may reflect a
300 parasite-specific behavioral consequence of rapid sensory adaptation that permits iL3s
301 to flexibly adjust their host-seeking behaviors after encountering a non-host heat
302 source.
303
304 **The Ss-AFD-rGCs each confer sensitivity to temperature ranges spanning**
305 **ambient and host body heat**
306 Next, we sought to identify molecular mechanisms that underlie the expanded
307 responsiveness of Ss-AFD to mammalian body temperatures. In $C.$ $elegans$, two of the
308 AFD-specific rGCs, Ce-GCY-18 and Ce-GCY-23, act as thermoreceptors[35]. Specifically,
309 misexpression of Ce-GCY-18 and Ce-GCY-23, but not Ce-GCY-8, can confer TAX-4-
310 dependent sensitivity to thermal stimuli[35]. We wanted to test whether the $S.$ $stercoralis$
311 AFD-rGCs (Ss-GCY-23.1, Ss-GCY-23.2, and Ss-GCY-23.3) are thermoreceptors, and if

8

312 so whether they display response properties that might contribute to the expanded
313 range of *Ss*-AFD responsiveness. We therefore ectopically expressed each *Ss*-AFD-
314 rGC in *C. elegans* ASE chemosensory neurons also expressing the YC3.60 calcium
315 sensor, then measured responses to naturalistic warming temperature ramps. *Ce*-ASE
316 was chosen as the ectopic expression site, rather than *Ce*-AFD, in order to examine the
317 thermosensory properties of the *Ss*-AFD-rGCs independent of mechanisms for *Ce*-
318 AFD-specific signal amplification[26,35].

320 We found that each *Ss*-AFD-rGC is capable of conferring thermosensitivity in *Ce*-ASE,
321 and that their functional properties differ from each other and from those of the *C.
322 elegans* AFD-rGCs (Fig. 4a,b, Fig. S10). For *Ss*-GCY-23.1 and *Ss*-GCY-23.3 ectopic
323 expression, the threshold (T^*_{ASE}) of temperature-evoked activity is near mammalian skin
324 temperature; *Ss*-GCY-23.2 expression results in thermosensitive activity with a T^*_{ASE}
325 near ambient cultivation temperature (Fig. 4c). Notably, all three *Ss*-AFD-rGCs confer
326 thermosensitivity up to host body temperatures. Across the *Ss*-AFD-rGCs, the
327 temperature driving maximal responses varies such that *Ss*-GCY-23.3 responses peak
328 at warmer temperatures than *Ss*-GCY-23.1 and *Ss*-GCY-23.2 (Fig. 4c). These results
329 suggest that changes in the functional properties of *Ss*-AFD-rGCs, including an
330 expanded responsiveness to mammalian body temperatures relative to *C. elegans*
331 homologs, may contribute to both parasite-specific encoding of thermal cues in *Ss*-AFD
332 and the preference of *S. stercoralis* iL3s for mammalian body heat.

Discussion

335 Here, we identify multiple parasite-specific molecular, cellular, and behavioral
336 adaptations in the thermosensory circuit of the human parasite *S. stercoralis*. We
337 present the first uses of single-cell genetic targeting and neural imaging methods in a
338 non-*Caenorhabditis* nematode, as well as the first direct demonstration of parasite-
339 specific neural encoding strategies that underlie sensory-driven host seeking by soil-
340 transmitted parasitic nematodes. Our results provide mechanistic insight into the neural
341 basis of heat seeking, an essential component of the ability of soil-transmitted parasitic
342 nematodes to target human hosts. Historically, most research on parasitic nematodes
343 has used the free-living nematode *Caenorhabditis elegans* as a genetically-tractable
344 model for human parasites. Our data indicate that this approach is not sufficient, and
345 emphasize the essential role of mechanistic studies in parasitic nematodes themselves
346 for understanding the neural basis of parasitism in these species. Parasitic nematode
347 infections are one of the world's most neglected sources of chronic disease and
348 economic burden; parasitic sensory circuits are a promising, yet largely unexplored,
349 target for intervention.

Figure Legends

352 **Figure 1. The *S. stercoralis* AFD neurons are required for positive thermotaxis
353 toward host body temperatures. a.** Tracks of *S. stercoralis* iL3s engaging in positive
354 thermotaxis toward host body temperatures. Worms were placed at 23°C in a ~21-33°C
355 gradient and allowed to migrate for 20 min. **b.** Phylogenetic tree of *C. elegans* AFD-
356 specific receptor-type guanylyl cyclases (AFD-rGCs, green text) and homologous
357 *S. stercoralis* (orange text) and *S. ratti* (purple text) proteins. Putative AFD-rGCs for

358   *Strongyloides spp.* were identified based on protein sequence homology with *C.*
359   *elegans* GCY-8, GCY-18, and GCY-23. SSTP and SRAE numbers indicate
360   *S. stercoralis* and *S. ratti* WormBase ParaSite gene IDs, respectively; gene names
361   indicating homology to *C. elegans* GCY-23 (GCY-23.1, GCY-23.2, and GCY-23.3) for *S.*
362   *stercoralis* and *S. ratti* sequences are shown in parentheses. **c.** The promoter region for
363   *Sr-gcy-23.2* drives GFP expression in a single neuron pair (top) with a dendritic
364   morphology (bottom left) that matches the lamellar morphology of *S. stercoralis*
365   ALD[11,32,33]. For top image, scale bar is 10 μm. For bottom left image, scale bar is 2 μm.
366   For all images, anterior is to the left. **d.** HisCl1-mediated silencing of the *S. stercoralis*
367   AFD neuron pair results in profound reductions in positive thermotaxis by iL3s. *Left:*
368   Tracks of *Sr-gcy-23.2p::strHisCl1*; *Sr-gcy-23.2p::GFP* iL3s treated with BU saline or
369   histamine (either 20 or 50 μL) in BU for at least 1 h, migrating in a ~22-34°C gradient for
370   10 min. T_{start} = 30°C. *Right:* Change in temperature, average speed, and distance ratio
371   (total distance ÷ maximum displacement) exhibited by individual iL3s. n = 38 worms for
372   iL3s treated with BU saline, 36 worms for histamine-treated iL3s; ****$p < 0.0001$, two-
373   sided Mann-Whitney test. Exact *p* values for all figures are provided in Supplemental
374   Data File 1. For all plots of worm tracks: Scale bar = 2 cm, gray zone = 1°C centered at
375   T_{start}. A subset of 10 randomly selected tracks are plotted and only a portion of the full
376   gradient is shown.

377

378   **Figure 2. Naturalistic warming ramps drive parasite-specific warming-triggered**
379   **hyperpolarizations followed by near-linear thermal encoding in *S. stercoralis* AFD**
380   **neurons. a.** *C. elegans* AFD and *S. stercoralis* AFD responses to a 20-34°C warming
381   temperature ramp that approximates the temperatures experienced by iL3s engaging in
382   positive thermotaxis in a ~22-34°C gradient. Colored traces show the responses of
383   individual worms; black traces show median responses. Heatmaps show responses
384   normalized to the maximum $\Delta R/R_0$ response for each species, with R_0 set to zero.
385   Responses are ordered by hierarchical cluster analysis. For all plots, temperature traces
386   show the average recorded temperature (mean in solid line, SD in shading; in some
387   cases, shading is too small to be visible). Warming ramp slope = 0.025 °C/s. R_0
388   (horizontal dotted lines) = response at 20°C. n = 15 worms for *S. stercoralis*, 20 for *C.*
389   *elegans*. **b.** Thermal threshold (T^*_{AFD}) of *C. elegans* and *S. stercoralis* AFD calcium
390   responses, where T^*_{AFD} is defined as the first temperature where $\Delta R/R_0$ is significantly
391   different from baseline (3 * STD R_0) for at least 10 seconds. Data are responses to
392   either a 20-34°C (circles) or a 20-40°C (squares) warming ramp. Meaningful differences
393   between *C. elegans* T^*_{AFD} and *S. stercoralis* T^*_{AFD} were not detected (difference
394   between median T^*_{AFD} = -0.2°C (*Ss*-AFD vs *Ce*-AFD), effect size = 0.187, power =
395   0.095, Mann-Whitney test). **c.** Temperature that elicits the lowest calcium response in
396   *Ce*-AFD and *Ss*-AFD, in response to either a 20-34°C (circles) or a 20-40°C (squares)
397   warming ramp. Horizontal dashed lines indicate T_C (23°C) and T_{min} (20°C).
398   ****$p < 0.0001$, Mann-Whitney test. **d.** Plots of % $\Delta R/R_0$ as a function of temperature at
399   near-ambient temperatures (20-25°C). Horizontal dotted line indicates R_0 (response at
400   20°C). **e.** Quantification of monotonic correlation between temperature and calcium
401   responses in the 20-25°C range. Values are Spearman's correlation coefficients.
402   ****$p < 0.0001$, Mann-Whitney test. **f.** Temperature that elicits the highest calcium
403   response in *Ce*-AFD and *Ss*-AFD, in response to a 20-34°C warming ramp. Horizontal

404 dashed line indicates the maximum temperature tested (T_{max}; 34°C). ****p<0.0001,
405 Mann-Whitney test. n = 15 worms for *S. stercoralis*, 20 for *C. elegans*. **g.** Plots of %
406 $\Delta R/R_0$ as a function of temperature at above-ambient temperatures (25-34°C).
407 Horizontal dotted line indicates R_0 (response at 20°C). **h.** Quantification of linear
408 correlation between temperature and calcium responses at 25°C and higher. Values are
409 Pearson's correlation coefficients. ****p<0.0001, Mann-Whitney test. For all plots: icons
410 indicate responses of individual worms, boxes show median and interquartile ranges,
411 whiskers show min and max values. T_C (ambient) = 23°C. n = 20 worms for *C. elegans*,
412 30 for *S. stercoralis*, unless otherwise specified. All Mann-Whitney tests are two-sided.
413
414 **Figure 3. *S. stercoralis* iL3s display rapid behavioral and neural adaptation in**
415 **response to thermosensory cues well below host body temperatures. a.** Example
416 tracks of individual *S. stercoralis* iL3s engaging in "reversal behavior," which is
417 characterized by an abrupt transition from sustained positive thermotaxis to sustained
418 negative thermotaxis. Gradient range: 15-25°C. T_{start} = 23°C. T_C = 23°C. Left: Example
419 worm tracks artificially distributed along the y-axis to increase visual clarity. Right:
420 Temperatures experienced by individual iL3s as a function of time; traces are the same
421 worms displayed in the left panel. Median time spent near T_{max} = 216 s (IQR = 166-244
422 s). n = 5 worms. **b.** Worms cultivated at 15°C also display reversal behaviors. Gradient
423 range: 12-22°C. T_{start} = 20°C. T_C = 15°C. Median time spent near T_{max} = 126 s (IQR =
424 106-150 s). n = 9 worms, plots show subset of tracks. Plots use same conventions as in
425 panel **a**. **c.** Percent of *S. stercoralis* iL3s engaging in positive thermotaxis (PT) that
426 reverse into negative thermotaxis. Annotations along the x-axis are the average
427 percentage of the total population that engages in positive thermotaxis under each
428 experimental condition. Boxes indicate medians and interquartile ranges; whiskers
429 indicate min and max values. n = 15 assays for the 15-25°C gradient when T_C = 15°C,
430 16 for all other conditions. ns = not significant (p>0.05), ****p<0.0001, Kruskal-Wallis
431 test with Dunn's post-test. **d.** Diagram of thermal stimulus that mimics temperature
432 ramps experienced by 15°C-cultivated iL3s displaying reversal behavior in a 12-22°C
433 gradient. These parameters were chosen because they are the assay conditions most
434 likely to elicit reversal behaviors. Ramp slope: ±0.025 °C/s. Holding time at 22°C = 5
435 min. **e.** *Ss*-AFD calcium responses to the thermal stimulus shown in panel **d**. For
436 calcium responses, colored lines indicate responses from individual worms, black line
437 indicates median response. Temperature traces are mean + SD recorded temperature
438 (lines + shading; in some cases, shading is too small to be visible). Dashed vertical line
439 indicates thermal threshold. Dotted horizontal line indicates baseline temperature
440 response, equivalent to the response at T_C (R_{Tc}). n = 17 worms. T_C = 15°C. **f.** *Ss*-AFD
441 calcium responses to different maximum temperatures (T_{max}): 22°C, 26°C, and 32°C.
442 Colored shading indicates time windows used for analyses in panels **g**, **h**. n = 17 worms
443 (22°C or 26°C), 16 worms (32°C). T_C = 15°C. All other conventions are the same as
444 panel **e**. **g.** Adaptation of the steady-state *Ss*-AFD calcium responses at different T_{max}
445 values. Calcium responses are calculated over two analysis windows: the early T_{max}
446 response (first 15 seconds) and the late T_{max} response (30 seconds - end). ns = not
447 significant (p>0.05), ***p<0.001, ****p<0.0001, two-way repeated-measures ANOVA
448 with Šidák's multiple comparisons tests. Boxes indicate medians and interquartile
449 ranges; whiskers indicate min and max values. n = 17 worms (22°C or 26°C), 16 worms

450 (32°C). T_C = 15°C. **h.** Temperature stimuli that are more likely to result in reversal
451 behaviors (*i.e.,* T_{max} = 22°C and T_{max} = 26°C vs T_{max} = 32°C) result in a higher
452 proportion of late T_{max} responses that are not significantly different from responses to
453 T_C. For each worm, significant T_{max} responses are those that vary from the average T_C
454 response by at least 3 standard deviations. 22°C vs 26°C: $p > 0.05$; 26°C vs 32°C:
455 $p > 0.05$; 22°C vs 32°C: $p < 0.0001$, Fisher's exact tests with Bonferroni-Dunn correction
456 for multiple comparisons. T_C = 15°C. All statistical tests are two-sided; when possible
457 we report multiplicity adjusted p values.

458
459 **Figure 4. All three *S. stercoralis* AFD-specific rGCs are thermoreceptors. a.**
460 Responses of *C. elegans* ASER/L neurons expressing YC3.60 and *Ss*-GCY-23.1 (left),
461 *Ss*-GCY-23.2 (middle), or *Ss*-GCY-23.3 (right) to naturalistic warming temperature
462 ramps. Warming stimulus ramp: 20-40°C at 0.025 °C/s. Vertical dashed lines indicate
463 average thermal threshold (T^*_{ASE}), defined as the first temperature where $\Delta R/R_0$
464 deviates from the average Ce-ASE_{WT} response by at least 3 * STD of ASE_{WT} $\Delta R/R_0$ for
465 a minimum of 40 seconds. Colored traces indicate responses of individual worms that
466 crossed the thermal threshold; gray traces indicate responses that did not. Black traces
467 show median responses; only worms with a response above threshold are included in
468 averages. Temperature traces show the average ± SD recorded temperature (lines +
469 shading; in some cases shading is too small to be visible). R_0 (horizontal dotted lines) =
470 response at 20°C. T_C = 23°C. n = 15 worms above threshold out of 17 total worms (*Ss*-
471 GCY-23.1), 14 of 15 worms (*Ss*-GCY-23.2), and 17 of 19 worms (*Ss*-GCY-23.3). **b.**
472 Heatmaps of individual *C. elegans* ASER/L responses from panel **a**. Responses are
473 normalized to the maximum $\Delta R/R_0$ response for each strain, with R_0 set to zero.
474 Responses are ordered by hierarchical cluster analysis. **c.** Thermal thresholds (left) and
475 temperatures eliciting highest calcium responses (right) for *C. elegans* ASE neurons
476 expressing *Ss-gcy-23.1* (purple icons), *Ss-gcy-23.2* (teal icons), and *Ss-gcy-23.3* (red
477 icons) measured in individual worms from three replicate strains (n = 5-17 worms per
478 strain). Only worms with a response crossing the thermal threshold are included in
479 quantifications. Boxes show medians and interquartile ranges, whiskers show min and
480 max values. Horizontal dashed line indicates T_{max} (40°C). n = 5-17 worms per strain,
481 with 26, 29, and 29 worms per genotype (*Ss*-GCY-23.1, *Ss*-GCY-23.2, and *Ss*-GCY-
482 23.3, respectively). **$p < 0.01$, ***$p < 0.001$, ****$p < 0.0001$, two-sided Kruskal-Wallis test
483 with Dunn's post-test; multiplicity adjusted p values are reported.

484
485 **Methods**
486 All protocols and procedures involving vertebrate animals were approved by the UCLA
487 Office of Animal Research Oversight (Protocol 2011-060-AM-003), which adheres to the
488 standards of the AAALAC and the *Guide for the Care and Use of Laboratory Animals*.

489
490 **Molecular Biology**
491 Identification of the following *S. stercoralis* and *S. ratti* genes was based on protein
492 sequence homology with *C. elegans* GCY-8, GCY-18, and GCY-23: *Ss-gcy-23.1*
493 (SSTP_0000354300), *Ss-gcy-23.2* (SSTP_0000775800)*, Ss-gcy-23.3*
494 (SSTP_0000846800)*, Sr-gcy-23.1* (SRAE_2000430600)*, Sr-gcy-23.2*
495 (SRAE_0000007100)*,* and *Sr-gcy-23.3* (SRAE_X000020900). Amino acid sequences

496 were retrieved from WormBase ParaSite[52]. Pairwise alignment of amino acid sequences
497 was calculated in Geneious Prime (v2020.1.1) using global alignment with free end
498 gaps and a Blosum62 cost matrix. Tree construction was performed in Geneious Prime
499 using a Jukes-Cantor model with neighbor-joining.
500
501 Promoter sequences for all *S. stercoralis* genes and *Sr-gcy-23.2* were extracted by
502 PCR-amplifying ~1.7-2 kb upstream of the predicted first exons; some sequences
503 include portions of the first exon. Primers used are listed in Supplemental Data File 2.
504 Putative promoter sequences were cloned into either the *Strongyloides* expression
505 vector pPV254 (containing *Ss-act-2p::GFP*; a gift from Dr. James Lok, UPenn) in place
506 of the *Ss-act-2* promoter, or into a *Strongyloides* promoter-less expression vector
507 (pASB10, which features a multiple cloning site and the *Ss-era-1* 3'UTR[39]) along with
508 *wrmScarlet-I*[53] (obtained from Dr. Hillel Schwartz, Caltech). The following constructs
509 were generated: *Ss-gcy-23.1p::GFP* (pASB51)*, Ss-gcy-23.2p::GFP* (pASB41)*, Ss-gcy-*
510 *23.3p::GFP* (pASB42)*, Sr-gcy-23.2p::GFP* (pJHL09)*, and Sr-gcy-23.2p::wrmScarlet-I*
511 (pASB25).
512
513 For expression of HisCl1 in *S. stercoralis* AFD, we first calculated a *Strongyloides*
514 codon-optimized *HisCl1* sequence (*strHisCl1*) by hand[42,54]. To generate a *Sr-gcy-*
515 *23.2p::strHisCl1* construct (pASB30), *strHisCl1* was synthesized by Genewiz (South
516 Plainfield, NJ) and cloned into pASB10 with the *Sr-gcy-23.2* promoter from pJHL09. For
517 expression of the calcium sensor YC3.60[43] in *S. stercoralis* AFD, we calculated a
518 *Strongyloides* codon-optimized *YC3.60* sequence (*strYC3.60*) by hand. To generate a
519 *Sr-gcy-23.2p::strYC3.60* construct (pASB52), *strYC3.60* was synthetized by Genewiz
520 and cloned into pASB30, replacing *strHisCl1*.
521
522 For ectopic expression of *S. stercoralis* AFD-rGCs in *C. elegans* ASE neurons, cDNA
523 sequences were identified based on gene predictions in WormBase ParaSite[52,55].
524 Sequences were codon-optimized for *C. elegans* and 2 synthetic introns were inserted
525 into the sequence using the *C. elegans* Codon Adapter[56]. To generate a *flp-6p::Ss-gcy-*
526 *23.1::SL2::mCherry* construct (pASB57), the cDNA sequence was synthesized by
527 Genewiz and used to modify the plasmid AT1_66, obtained from Dr. Piali Sengupta
528 (Brandeis)[35]. To generate *flp-6p::Ss-gcy-23.2::SL2::mCherry* (pASB61) and *flp-6p::Ss-*
529 *gcy-23.3::SL2::mCherry* (pASB62) constructs, cDNA sequences were synthesized and
530 inserted into AT1_66 by GenScript (Piscataway, NJ). A full list of all plasmids used in
531 this study are provided in Supplemental Data File 2.
532
533 **Strains**
534 *S. stercoralis* (UPD strain) was maintained as previously described[10]. Transgenic
535 *S. stercoralis* F_1 iL3s were generated by microinjection of plasmid constructs into free-
536 living adult females using standard methods[39]. Fecal-charcoal plates containing
537 microinjected females and wild-type adult males were incubated at 23°C for a minimum
538 of 5 days prior to screening and experimental use. To generate transgenic F_1 iL3s
539 expressing fluorescent reporters, plasmids (including: pJHL09, pASB25, pASB41,
540 pASB42, pASB51, and pMLC41[10]) were microinjected at 40-100 ng/µL (Supplemental
541 Data File 2). Targeted mutagenesis of *Ss-tax-4* was accomplished using established

13

542   *Strongyloides* CRISPR/Cas9 protocols[10,47], with the following modifications. For
543   generating *Ss-tax-4* iL3s, injection mixes contained 80 ng/μL pMLC47, 80 ng/μL pEY11,
544   and 40 ng/μL pPV540. For generating no-Cas9 controls, injection mixes contained 80
545   ng/μL pMLC47 and 80 ng/μL pEY11. For calcium imaging of *S. stercoralis* AFD, *Sr-gcy-*
546   *23.2p::strYC3.60* F_1 iL3s were generated by microinjecting pASB52 at a concentration
547   of 80 ng/μL. For generating *Sr-gcy-23.2p::strHisCl1* iL3s, injection mixes contained 80
548   or 100 ng/μL pASB30 with 50 ng/μL pJHL09 as a co-injection marker.
549

550   *C. elegans* adults were raised on 2% Nematode Growth Media (NGM) plates seeded
551   with a lawn of *Escherichia coli* OP50 bacteria, as per standard methods[57]. *C. elegans*
552   experiments exclusively used young adult hermaphrodites; adult males were used only
553   for crosses. Calcium imaging of *C. elegans* AFD was performed using strain IK890
554   (*njEx358[gcy-8::YC3.60, ges-1::NLS-tagRFP]*), which was obtained from Dr. Ikue Mori
555   (Nagoya University). Calcium imaging of *C. elegans* ASE was performed using strain
556   XL115 *lin-15(n765) ntIs14[flp-6::YC3.60; lin-15+]*, which was obtained from Dr. Shawn
557   Lockery (U. Oregon). Independent strains for ectopic expression of *S. stercoralis* AFD-
558   rGCs in *C. elegans* ASE (Supplemental Data File 2, strains EAH359-EAH379) were
559   generated by microinjecting test plasmids (pASB57, pASB61, pASB62) into N2
560   hermaphrodites at 20 ng/μL. Each ectopic expression strain was crossed to XL115 to
561   generate the strains used for calcium imaging (Supplemental Data File 2, strains
562   EAH360-EAH380).
563

Fluorescent Microscopy
565   For fluorescent microscopy, the F_1 iL3 progeny of microinjected females were recovered
566   and screened for GFP or wrmScarlet-I expression on a Leica M165 FC fluorescence
567   microscope using a previously established nicotine-paralysis method[47]. Transgenic iL3s
568   were transferred to a small watch glass containing BU saline[58] and allowed to recover
569   overnight. Animals were exposed to 50-100 mM levamisole in BU saline, then mounted
570   on a slide with 5% Noble agar dissolved in BU saline, coverslipped, and sealed with
571   quick-drying nail polish. Epifluorescence and DIC images were taken using a Zeiss
572   AxioImager A2 microscope with an attached Hamamatsu ORCA-Flash camera
573   (C13440-20CU-KIT Flash4.0 V3 sCMOS). Confocal images were acquired using a
574   Zeiss LSM880 confocal microscope (Broad Stem Cell Research Center, Molecular,
575   Cellular, and Developmental Biology Microscopy Core Facility, UCLA). Images were
576   processed using the Zeiss Zen pro software (v2.6). Image montages were generated
577   using FIJI.
578

Behavioral Assays
580   Thermotaxis assays were performed using a custom thermoelectric behavioral arena[10].
581   For experiments quantifying the distribution of a population, worms were monitored
582   using one or two 5 mega-pixel CMOS cameras (BTE-BO50-U, Mightex Systems) at a
583   frame rate of at least 1 frame per minute. The population-level movement of worms was
584   analyzed as previously described[10]. For worm tracking experiments, worm movements
585   were imaged at a frame rate of 0.5 frames per second, and individual iL3 trajectories
586   were quantified *post hoc* as previously described[10], using updated custom MATLAB
587   scripts.

14

588
589 For testing wild-type thermotaxis behaviors across different cultivation temperatures,
590 iL3s were collected from 7-14 day old fecal-charcoal plates using a Baermann
591 apparatus[59] or removed directly from the fecal charcoal lid and then stored in a watch
592 glass containing BU saline at either 15°C or 23°C for at least two hours. For negative
593 thermotaxis behaviors, iL3s were placed in a 12-22°C gradient (T_{start} = 14°C, 17°C, or
594 20°C) for 30 minutes. For positive thermotaxis behaviors, iL3s were placed in a ~21-
595 33°C gradient (T_{start} = 23°C) for 20 minutes. The behavioral data for unstimulated wild-
596 type iL3s (Fig. S2b) are from Bryant *et al* 2018[10].

597
598 For measuring reversal behaviors, 7-14 day old fecal-charcoal plates were incubated for
599 at least two hours at 15°C or 23°C. iL3s were collected using a Baermann apparatus or
600 removed directly from the lid of the fecal-charcoal plate and stored in a watch glass
601 containing BU saline at their cultivation temperature for at least two hours. Two thermal
602 gradients were used to elicit reversal behaviors: a 12-22°C gradient (T_{start} = 20°C) and a
603 15-25°C gradient (T_{start} = 23°C). For testing the percentage of the population that
604 engaged in reversal behaviors, at least 150 iL3s were placed on a thermotaxis plate and
605 their migration was imaged for 20-30 minutes. For tracking individual iL3 trajectories
606 during reversal behaviors, either single iL3s or a small group (<100) of iL3s were placed
607 on a thermotaxis plate and their migration was imaged for 20 min.

608
609 For testing negative thermotaxis by *Ss-tax-4* iL3s, either *Ss-tax-4* iL3s or no-Cas9
610 control iL3s were screened for mRFPmars expression as previously described[10,47]. 1-2
611 mRFPmars-expressing *S. stercoralis* iL3s were placed at 20°C in a ~17-26°C gradient
612 for 15 min. Following the cessation of recording, single iL3s were recollected for
613 individual genomic DNA preparations. mRFPmars-positive iL3s in which *Ss-tax-4*
614 expression was fully disrupted either by deletion or integration events (*i.e.*, *Ss-tax-4*
615 iL3s) were identified by *post-hoc* single-worm genotyping, as previously described[10,47].
616 Trajectories of *Ss-tax-4* iL3s were tracked and quantified following *post-hoc* genotyping.

617
618 For testing the effect of HisCl1-mediated AFD silencing on positive and negative
619 thermotaxis, *Sr-gcy-23.2p::strHisCl1* + *Sr-gcy-23.2p::GFP* iL3s were screened for GFP
620 expression as follows: F_1 iL3 progeny of microinjected females were recovered from
621 fecal-charcoal cultures using a Baermann apparatus and stored in a small watch glass
622 containing 2-3 mL BU saline. ~10 μL of iL3-containing BU saline was placed on a 2%
623 NGM plate containing a lawn of OP50, and migrating iL3s were screened at low
624 magnification for strong GFP expression. Recovered iL3s were evenly split into two
625 watch glasses containing either BU saline or BU saline + either 20 or 50 mM histamine.
626 Watch glasses were incubated at 23°C for at least 2 h. For behavioral experiments, iL3s
627 were transferred in batches (<20 worms per experiment) to 3% thermotaxis agar
628 plates[10,60] with or without 10 mM histamine. For positive thermotaxis assays, iL3s were
629 placed at 30°C in an ~22-34°C gradient; for negative thermotaxis assays, iL3s were
630 placed at 20°C in a ~17-26°C gradient. For both positive and negative thermotaxis,
631 assay duration was 10 min. On individual experimental days, behavioral assays were
632 always conducted with paired histamine-positive and no-histamine control experiments.
633 Furthermore, the researcher performing the assay was fully blinded to the experimental

634 condition: blinding was implemented as recovered GFP-positive iL3s were split into BU
635 saline or BU saline + histamine watch glasses (*i.e.,* the researcher splitting the
636 population was unaware of which watch glass contained histamine-spiked BU saline).
637 Blinding was lifted only following *post-hoc* tracking.
638
639 **Calcium Imaging**
640 For calcium imaging of *Ss*-AFD, the F_1 iL3 progeny of microinjected females were
641 recovered and screened for the presence of YC3.60 using methods previously
642 established for fluorescent screening of nicotine-paralyzed transgenic iL3s[47]. Prior to
643 calcium imaging, *C. elegans* adults on 2% NGM plates with an OP50 lawn or *S.*
644 *stercoralis* iL3s in BU saline-containing watch glasses were incubated overnight at
645 either 23°C or 15°C. Animals were exposed to 100 mM levamisole in BU saline (*S.*
646 *stercoralis* iL3s) or 10 mM levamisole in M9 saline (*C. elegans* adults), then mounted on
647 a slide with 5% Noble agar dissolved in BU or M9 saline, coverslipped, and sealed with
648 quick-drying nail polish.
649
650 Calcium imaging was performed using a Zeiss AxioImager A2 microscope equipped
651 with a 78 HE ms CFP/YFP dual camera filter set, a Hamamatsu W-View Gemini image
652 splitter, and a Hamamatsu ORCA-Flash camera for simultaneous acquisition of CFP
653 and YFP images. Images were acquired every 250 ms using the Zeiss ZEN software
654 with a time lapse module.
655
656 Temperature ramps were delivered to slide-mounted worms using a custom thermal
657 stimulator (Fig. S3a) based on established *C. elegans* systems[46]. An annular-style
658 Peltier element (430533-502, Laird Thermal Systems) was mounted on a custom
659 aluminum heat block held on the microscope stage with a custom 3D-printed stage
660 clamp. The custom heat block was attached to a temperature-controlled recirculating
661 water bath (13-874-180, Fisher Scientific) set to the cultivation temperature. The Peltier
662 element was controlled by a closed-loop control circuit consisting of a PID controller
663 (ATEC302, Accuthermo Technology), an H-bridge amplifier (FTX700D, Accuthermo
664 Technology), two 12 V, 30 W AC/DC power converters (LS35-12, TDK-Lambda
665 Americas Inc), and a 10 kΩ thermistor (USP12837, Littelfuse) that was attached to the
666 coverslip near the immobilized worm with adhesive tape. Slides containing worms were
667 placed on the Peltier element; halocarbon oil was placed between the Peltier element
668 and the glass slide to ensure strong thermal transfer. Slides were anchored to the
669 aluminum heat block using adhesive tape. Prior to the start of imaging, slides were
670 brought to cultivation temperature (23°C or 15°C) for 5 min using the ATEC302 software
671 general control mode. During imaging, temperature ramps were delivered using the
672 ATEC302 software programmable step temperature control function. A full list of all
673 thermal ramps used in this study is provided in Supplemental Data File 2. Measured
674 temperatures at the coverslip surface were recorded using the ATEC302 software data
675 log function.
676
677 From time-lapse dual-wavelength images containing aligned CFP and YFP signals we
678 calculated the mean intensity over time for soma and background regions of interest
679 (ROI) using the ZEN software. CSV files containing imaging data and temperature log

680 files were saved, then processed using custom MATLAB scripts. Briefly, CFP and YFP
681 signals from soma and background ROIs were used to calculate the baseline-corrected
682 YFP/CFP ratio (% $\Delta R/R_0$); YFP signals were corrected for bleed-through from the CFP
683 channel. Calcium responses were aligned relative to the ATEC302 temperature log
684 based on file time stamps. Plots of aligned calcium responses and temperature records
685 were saved as EPS files. For heatmaps, individual calcium traces (heatmap rows) were
686 ordered using average linkage clustering; heatmap colors were defined using the viridis
687 color map.
688
689 Custom MATLAB code was used to calculate: linear/monotonic regressions at different
690 temperature windows, thermal threshold (either T^*_{AFD} or T^*_{ASE}), temperatures eliciting
691 maximal and minimal calcium responses, and the response magnitude at the hottest
692 stimulus temperature (T_{max}) or the coolest stimulus temperature (T_{min}), across different
693 time windows. For AFD recordings, thermal threshold (T^*_{AFD}) is defined as the first
694 temperature where the absolute value of the AFD response is at least 3*STD from the
695 response at T_0 for the amount of time it takes the warming/cooling temperature ramp to
696 change 0.25°C (either 2.5 or 10 s). For *C. elegans* ectopic expression recordings,
697 thermal threshold (T^*_{ASE}) was defined as the first temperature where the absolute value
698 of the *Ce*-ASE_{experimental} response deviates from the average *Ce*-ASE_{WT} response by at
699 least 3*STD of the *Ce*-ASE_{WT} response for a minimum of 40 seconds.
700
701 **Quantification and Statistical Analysis**
702 Statistical analyses were conducted using GraphPad Prism 9. Exact *p* values for all
703 statistical tests are provided in Supplemental Data File 1. Power analyses to determine
704 appropriate sample sizes were conducted using G*Power 3.1. For plotting single-worm
705 tracking quantifications and calcium imaging quantifications, data were imported into R
706 v3.6.3 and plotted using the ggplot2 package v3.3.2[61].
707
708 **Data Availability**
709 The data that support the findings of this study are available on GitHub
710 (https://github.com/HallemLab/Bryant_et_al_2021).
711
712 **Code Availability**
713 Source code for the following tasks is available on GitHub: acquisition, analysis, and
714 plotting of single worm tracks; preprocessing calcium imaging data; and plotting
715 quantifications from worm tracking and calcium imaging experiments
716 (https://github.com/HallemLab/Bryant_et_al_2021). Parts lists and wiring diagrams for
717 custom hardware are also available in the same GitHub repository.
718
719 **References**
720 1. Beknazarova, M., Whiley, H. & Ross, K. Strongyloidiasis: a disease of socioeconomic
721 disadvantage. *Int J Environ Res Public Health* **13**, 517 (2016).
722 2. Bethony, J. *et al.* Soil-transmitted helminth infections: ascariasis, trichuriasis, and hookworm.
723 *Lancet* **367**, 1521–1532 (2006).
724 3. Lustigman, S. *et al.* A research agenda for helminth diseases of humans: the problem of
725 helminthiases. *PLoS Negl Trop Dis* **6**, e1582 (2012).

4. McKenna, M. L. *et al.* Human intestinal parasite burden and poor sanitation in rural Alabama. *Am J Trop Med Hyg* **97**, 1623–1628 (2017).

5. Singer, R. *et al.* Prevalence of intestinal parasites in a low-income Texas community. *Am J Trop Med Hyg* **102**, 1386–1395 (2020).

6. Nutman, T. B. Human infection with *Strongyloides stercoralis* and other related *Strongyloides* species. *Parasitology* **144**, 263–273 (2017).

7. Schafer, T. W. & Skopic, A. Parasites of the small intestine. *Curr Gastroenterol Rep* **8**, 312–320 (2006).

8. Buonfrate, D. *et al.* Severe strongyloidiasis: a systematic review of case reports. *BMC Infect Dis* **13**, 78 (2013).

9. Bryant, A. S. & Hallem, E. A. Terror in the dirt: Sensory determinants of host seeking in soil-transmitted mammalian-parasitic nematodes. *Int J Parasitol Drugs Drug Resist* **8**, 496–510 (2018).

10. Bryant, A. S. *et al.* A critical role for thermosensation in host seeking by skin-penetrating nematodes. *Curr Biol* **28**, 2338–2347 (2018).

11. Bryant, A. S. & Hallem, E. A. Temperature-dependent behaviors of parasitic helminths. *Neurosci Lett* **687**, 290–303 (2018).

12. Buonfrate, D. *et al.* The global prevalence of *Strongyloides stercoralis* infection. *Pathogens* **9**, 468 (2020).

13. Tamarozzi, F. *et al.* Morbidity associated with chronic *Strongyloides stercoralis* infection: a systematic review and meta-analysis. *Am J Trop Med Hyg* **100**, 1305–1311 (2019).

14. De Wilton, A. *et al.* Risk of *Strongyloides* Hyperinfection Syndrome when prescribing dexamethasone in severe COVID-19. *Travel Med Infect Dis* **40**, 101981 (2021).

15. Stauffer, W. M., Alpern, J. D. & Walker, P. F. Covid-19 and dexamethasone: a potential strategy to avoid steroid-related *Strongyloides* hyperinfection. *JAMA* **324**, 623–624 (2020).

16. Diawara, A., Schwenkenbecher, J. M., Kaplan, R. M. & Prichard, R. K. Molecular and biological diagnostic tests for monitoring benzimidazole resistance in human soil-transmitted helminths. *Am J Trop Med Hyg* **88**, 1052–1061 (2013).

17. Keiser, J. & Utzinger, J. Efficacy of current drugs against soil-transmitted helminth infections: systematic review and meta-analysis. *JAMA* **299**, 1937–1948 (2008).

18. Learmount, J., Stephens, N., Boughtflower, V., Barrecheguren, A. & Rickell, K. The development of anthelmintic resistance with best practice control of nematodes on commercial sheep farms in the UK. *Vet Parasitol* **229**, 9–14 (2016).

19. Repetto, S. A. *et al.* Strongyloidiasis outside endemic areas: long-term parasitological and clinical follow-up after ivermectin treatment. *Clin Infect Dis* **66**, 1558–1565 (2018).

20. Gang, S. S. *et al.* Chemosensory mechanisms of host seeking and infectivity in skin-penetrating nematodes. *Proc Natl Acad Sci USA* **117**, 17913–17923 (2020).

21. Hedgecock, E. M. & Russell, R. L. Normal and mutant thermotaxis in the nematode *Caenorhabditis elegans*. *Proc Natl Acad Sci USA* **72**, 4061–4065 (1975).

22. Wittenburg, N. & Baumeister, R. Thermal avoidance in *Caenorhabditis elegans*: an approach to the study of nociception. *Proc Natl Acad Sci USA* **96**, 10477–10482 (1999).

23. Glauser, D. A. *et al.* Heat avoidance is regulated by transient receptor potential (TRP) channels and a neuropeptide signaling pathway in *Caenorhabditis elegans*. *Genetics* **188**, 91–103 (2011).

24. Garrity, P. A., Goodman, M. B., Samuel, A. D. & Sengupta, P. Running hot and cold: behavioral strategies, neural circuits, and the molecular machinery for thermotaxis in *C. elegans* and *Drosophila*. *Genes Dev.* **24**, 2365–2382 (2010).

25. Schild, L. C. & Glauser, D. A. Dynamic switching between escape and avoidance regimes reduces *Caenorhabditis elegans* exposure to noxious heat. *Nat Commun* **4**, 2198 (2013).

26. Goodman, M. B. & Sengupta, P. The extraordinary AFD thermosensor of *C. elegans*. *Pflugers Arch* **470**, 839–849 (2018).

27. Takeishi, A., Takagaki, N. & Kuhara, A. Temperature signaling underlying thermotaxis and cold tolerance in *Caenorhabditis elegans*. *J Neurogenet* **34**, 351–362 (2020).

28. Mori, I. & Ohshima, Y. Neural regulation of thermotaxis in *Caenorhabditis elegans*. *Nature* **376**, 344–348 (1995).

29. Chung, S. H., Clark, D. A., Gabel, C. V., Mazur, E. & Samuel, A. D. T. The role of the AFD neuron in *C. elegans* thermotaxis analyzed using femtosecond laser ablation. *BMC Neurosci* **7**, 30 (2006).

30. Luo, L. *et al.* Bidirectional thermotaxis in *Caenorhabditis elegans* is mediated by distinct sensorimotor strategies driven by the AFD thermosensory neurons. *Proc Natl Acad Sci USA* **111**, 2776–2781 (2014).

31. Wasserman, S. M., Beverly, M., Bell, H. W. & Sengupta, P. Regulation of response properties and operating range of the AFD thermosensory neurons by cGMP signaling. *Curr Biol* **21**, 353–362 (2011).

32. Ashton, F. T., Bhopale, V. M., Fine, A. E. & Schad, G. A. Sensory neuroanatomy of a skin-penetrating nematode parasite: *Strongyloides stercoralis*. I. Amphidial neurons. *J Comp Neurol* **357**, 281–295 (1995).

33. Lopez, P. M., Boston, R., Ashton, F. T. & Schad, G. A. The neurons of class ALD mediate thermotaxis in the parasitic nematode, *Strongyloides stercoralis*. *Int J Parasitol* **30**, 1115–1121 (2000).

34. Ashton, F. T., Li, J. & Schad, G. A. Chemo- and thermosensory neurons: structure and function in animal parasitic nematodes. *Vet Parasitol* **84**, 297–316 (1999).

35. Takeishi, A. *et al.* Receptor-type guanylyl cyclases confer thermosensory responses in *C. elegans*. *Neuron* **90**, 235–244 (2016).

36. Ramot, D., MacInnis, B. L. & Goodman, M. B. Bidirectional temperature-sensing by a single thermosensory neuron in *C. elegans*. *Nat Neurosci* **11**, 908–915 (2008).

37. Inada, H. *et al.* Identification of guanylyl cyclases that function in thermosensory neurons of *Caenorhabditis elegans*. *Genetics* **172**, 2239–2252 (2006).

38. Wang, D., O'Halloran, D. & Goodman, M. B. GCY-8, PDE-2, and NCS-1 are critical elements of the cGMP-dependent thermotransduction cascade in the AFD neurons responsible for *C. elegans* thermotaxis. *J Gen Physiol* **142**, 437–449 (2013).

39. Junio, A. B. *et al. Strongyloides stercoralis*: cell- and tissue-specific transgene expression and co-transformation with vector constructs incorporating a common multifunctional 3' UTR. *Exp Parasitol* **118**, 253–265 (2008).

40. Lok, J. B., Shao, H., Massey, H. C. & Li, X. Transgenesis in *Strongyloides* and related parasitic nematodes: historical perspectives, current functional genomic applications and progress towards gene disruption and editing. *Parasitology* **144**, 327–342 (2017).

41. Castelletto, M. L., Gang, S. S. & Hallem, E. A. Recent advances in functional genomics for parasitic nematodes of mammals. *J Exp Biol* **223**, jeb206482 (2020).

42. Pokala, N., Liu, Q., Gordus, A. & Bargmann, C. I. Inducible and titratable silencing of *Caenorhabditis elegans* neurons *in vivo* with histamine-gated chloride channels. *Proc Natl Acad Sci USA* **111**, 2770–2775 (2014).

43. Nagai, T., Yamada, S., Tominaga, T., Ichikawa, M. & Miyawaki, A. Expanded dynamic range of fluorescent indicators for Ca2+ by circularly permuted yellow fluorescent proteins. *Proc Natl Acad Sci USA* **101**, 10554–10559 (2004).

44. Clark, D. A., Biron, D., Sengupta, P. & Samuel, A. D. T. The AFD sensory neurons encode multiple functions underlying thermotactic behavior in *Caenorhabditis elegans*. *J Neurosci* **26**, 7444–7451 (2006).

45. Kimura, K. D., Miyawaki, A., Matsumoto, K. & Mori, I. The *C. elegans* thermosensory neuron AFD responds to warming. *Curr Biol* **14**, 1291–1295 (2004).

46. Hawk, J. D. *et al.* Integration of plasticity mechanisms within a single sensory neuron of *C. elegans* actuates a memory. *Neuron* **97**, 356–367 (2018).

47. Gang, S. S. *et al.* Targeted mutagenesis in a human-parasitic nematode. *PLoS Pathog* **13**, e1006675 (2017).

48. Komatsu, H., Mori, I., Rhee, J. S., Akaike, N. & Ohshima, Y. Mutations in a cyclic nucleotide-gated channel lead to abnormal thermosensation and chemosensation in *C. elegans*. *Neuron* **17**, 707–718 (1996).

49. Coburn, C. M. & Bargmann, C. I. A putative cyclic nucleotide-gated channel is required for sensory development and function in *C. elegans*. *Neuron* **17**, 695–706 (1996).

50. Biron, D. *et al.* A diacylglycerol kinase modulates long-term thermotactic behavioral plasticity in *C. elegans*. *Nat Neurosci* **9**, 1499–1505 (2006).

51. Yu, Y. V. *et al.* CaMKI-Dependent regulation of sensory gene expression mediates experience-dependent plasticity in the operating range of a thermosensory neuron. *Neuron* **84**, 919–926 (2014).

52. Howe, K. L., Bolt, B. J., Shafie, M., Kersey, P. & Berriman, M. WormBase ParaSite – a comprehensive resource for helminth genomics. *Mol Biochem Parasitol* **215**, 2–10 (2017).

53. El Mouridi, S. *et al.* Reliable CRISPR/Cas9 genome engineering in *Caenorhabditis elegans* using a single efficient sgRNA and an easily recognizable phenotype. *G3* **7**, 1429–1437 (2017).

54. Mitreva, M. *et al.* Codon usage patterns in Nematoda: analysis based on over 25 million codons in thirty-two species. *Genome Biol* **7**, R75 (2006).

55. Hunt, V. L. *et al.* The genomic basis of parasitism in the *Strongyloides* clade of nematodes. *Nat Genet* **48**, 299–307 (2016).

56. Redemann, S. *et al.* Codon adaptation-based control of protein expression in *C. elegans*. *Nat Methods* **8**, 250–252 (2011).

57. Stiernagle, T. Maintenance of *C. elegans*. *WormBook* 1–11, http://www.wormbook.org (2006) doi:10.1895/wormbook.1.101.1.

58. Hawdon, J. M. & Schad, G. A. Long-term storage of hookworm infective larvae in buffered saline solution maintains larval responsiveness to host signals. *J Helm Soc Wash* **58**, 140–142 (1991).

59. Lok, J. B. *Strongyloides stercoralis*: a model for translational research on parasitic nematode biology. *WormBook* 1–18 (2007) doi:10.1895/wormbook.1.134.1.

60. Goodman, M. B. Thermotaxis navigation behavior. *WormBook* 1–10 (2014) doi:10.1895/wormbook.1.168.1.

61. Wickham, H. *Ggplot2: elegant graphics for data analysis*. (Springer, 2009).

Acknowledgements

Author Contributions

A.S.B. and E.A.H. conceived the study and wrote the manuscript. A.S.B., F.R., and J.L. performed all experiments and analyzed the data. All authors read and approved the final manuscript.

20

877 **<u>Competing Interests</u>**

878 The authors declare no competing interests.

879

880 **<u>Corresponding Author</u>**

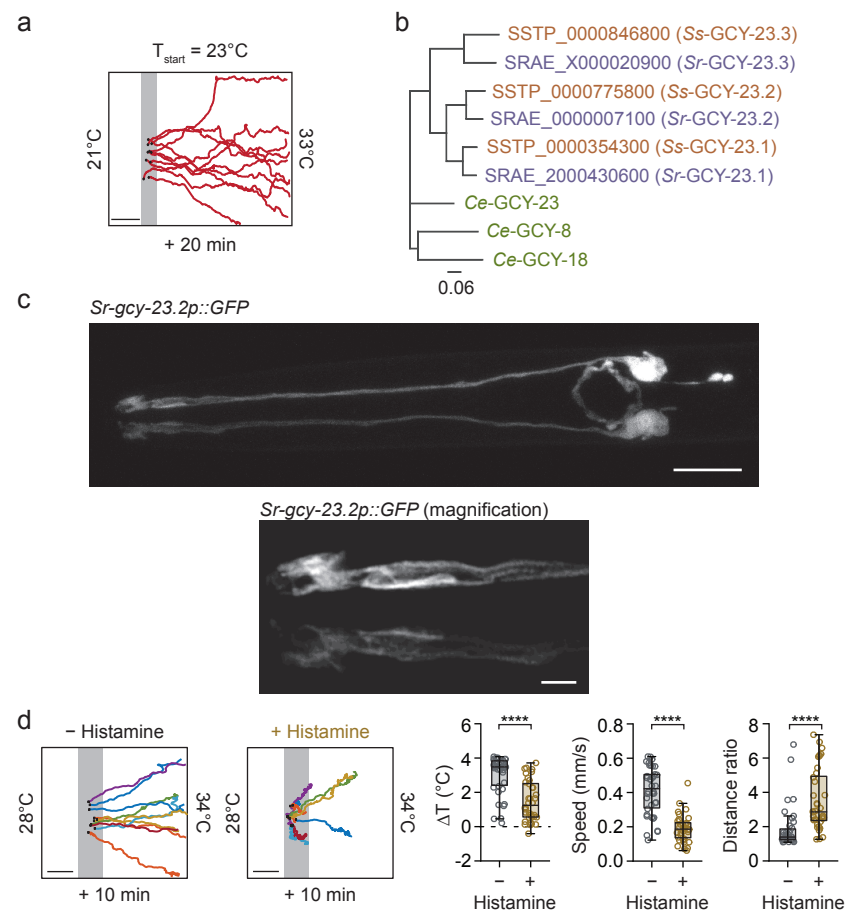881 Correspondence to Elissa A. Hallem.

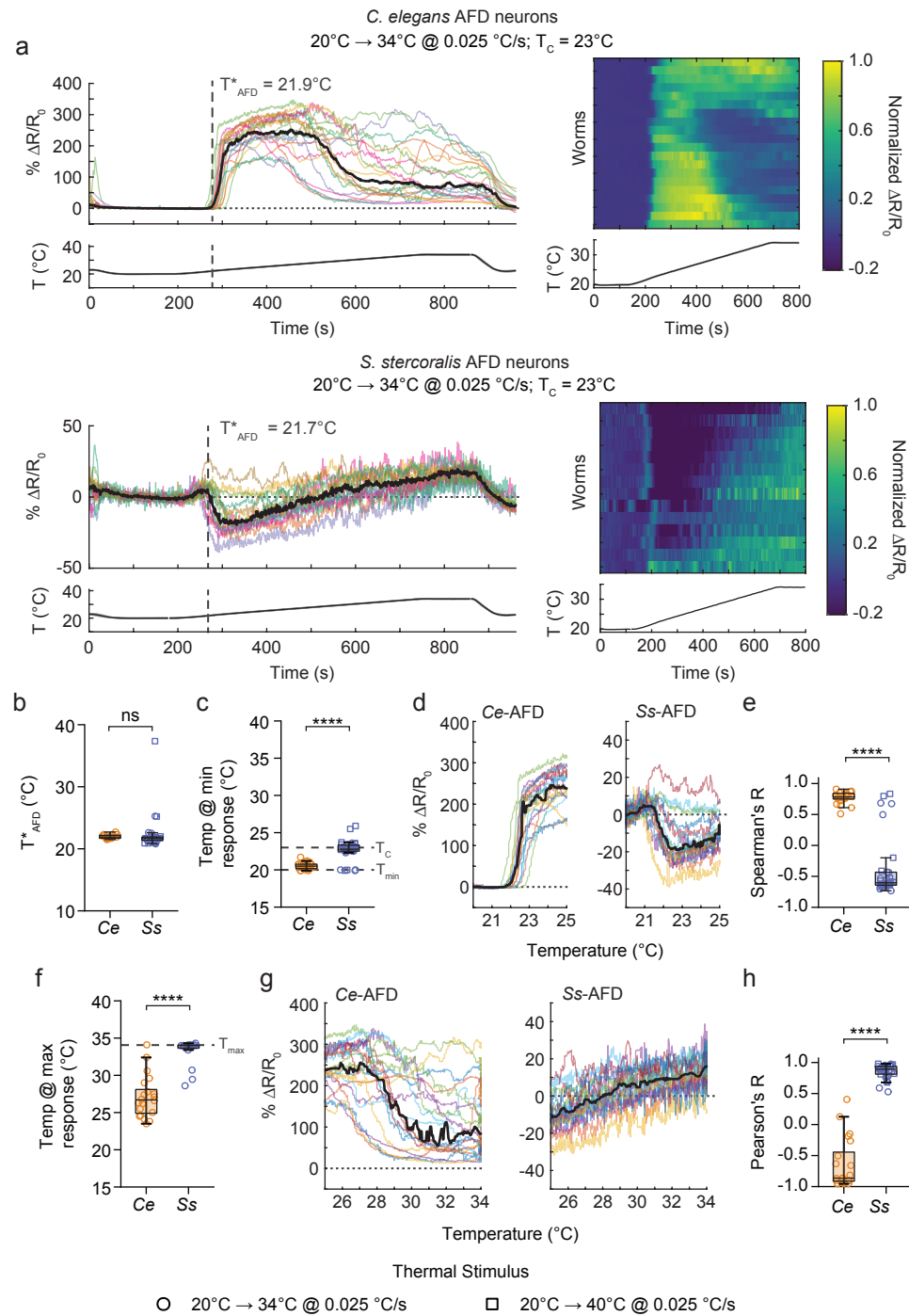Figure 1

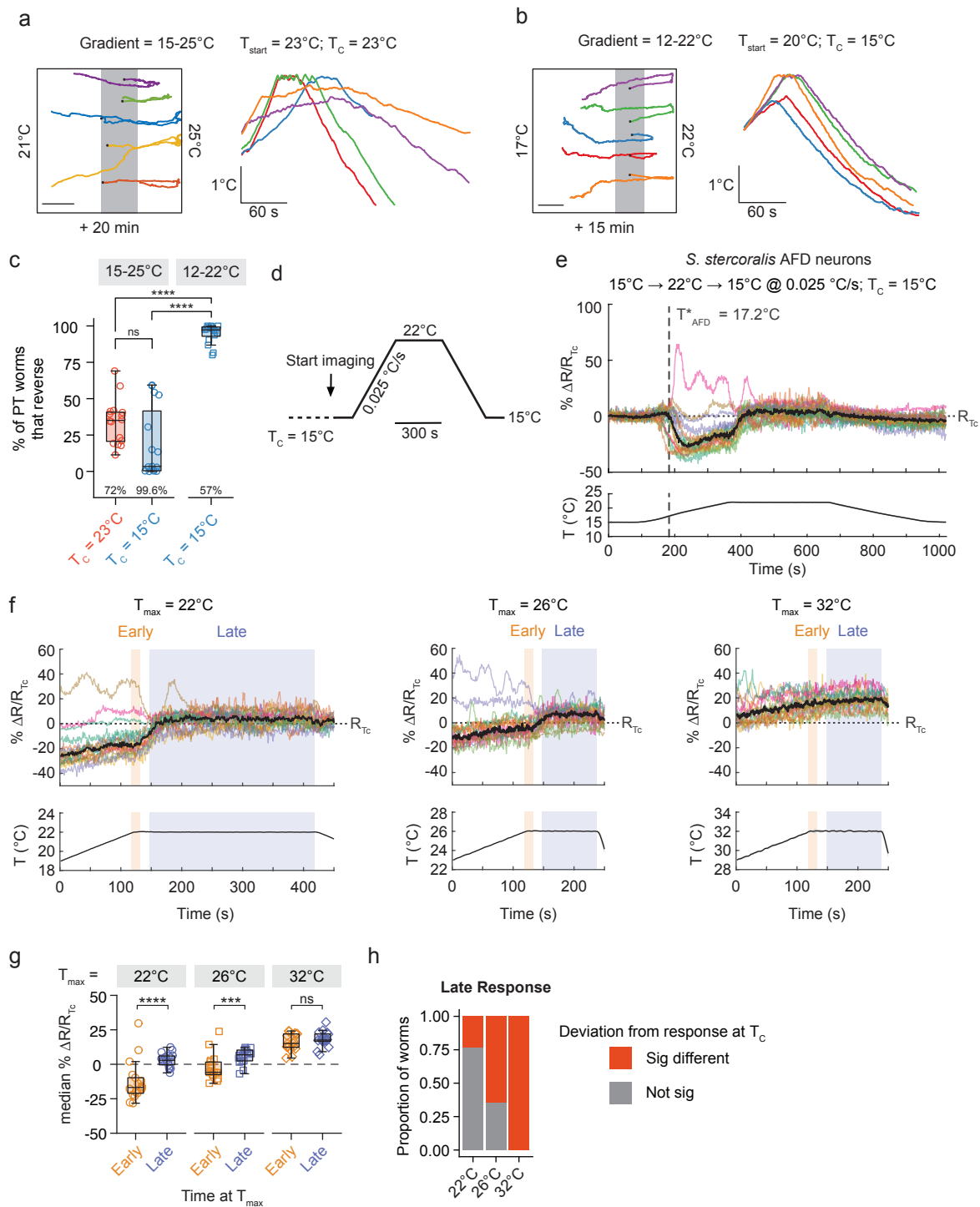Figure 2

a *C. elegans* AFD neurons
20°C → 34°C @ 0.025 °C/s; T_C = 23°C

S. stercoralis AFD neurons
20°C → 34°C @ 0.025 °C/s; T_C = 23°C

Thermal Stimulus

○ 20°C → 34°C @ 0.025 °C/s   □ 20°C → 40°C @ 0.025 °C/s

Figure 3

Figure 4

a

C. elegans ASE neurons
20°C → 40°C @ 0.025 °C/s; T_C = 23°C

Ce-flp-6p::Ss-gcy-23.1   *Ce-flp-6p::Ss-gcy-23.2*   *Ce-flp-6p::Ss-gcy-23.3*

T^*_{ASE} = 31.9°C T^*_{ASE} = 23.05°C T^*_{ASE} = 35.2°C

b

Ss-GCY-23.1

Ss-GCY-23.2

Ss-GCY-23.3

c

rGC
Ss-GCY-23.1
Ss-GCY-23.2
Ss-GCY-23.3

Strain
○ EAH360   ○ EAH368   ○ EAH375
□ EAH362   □ EAH371   □ EAH377
◇ EAH366   ◇ EAH373   ◇ EAH380